Electron Spin Coherence in Silicon Vacancy Defects of Proton-irradiated Silicon Carbide

Jacob Steven Embley

A senior thesis submitted to the faculty of
Brigham Young University
in partial fulfillment of the requirements for the degree of

Bachelor of Science

John S. Colton, Advisor

Department of Physics and Astronomy

Brigham Young University

April 2016

ABSTRACT

Electron Spin Coherence in Silicon Vacancy Defects of
Proton-irradiated Silicon Carbide

Jacob Steven Embley
Department of Physics and Astronomy, BYU
Bachelor of Science

Electron spin states in silicon carbide have shown potential for use as qubits. A qubit requires a quantum state that will remain coherent over a sufficiently long period of time. By measuring spin coherence times for electrons in silicon vacancies, we not only investigate their potential for use as qubits, but we better understand the factors which lead to their eventual decoherence. Using a combination of experimental techniques, including optically detected magnetic resonance and spin echo, we measured electron spin coherence times for two samples of proton-irradiated 4H-silicon carbide. Each sample was studied over a range of temperatures. Results indicate that the longest coherence times for each sample exist at the lowest temperature (8 K). While in general higher temperatures resulted in shorter coherence times, results also show a range of temperature from 60 K to 160 K for which the trend was reversed.

Keywords: electron spin coherence, silicon carbide, spin echo, optically detected magnetic resonance, silicon vacancies

ACKNOWLEDGMENTS

The production of the research presented in this thesis has been a marvelous experience for me, but it never could have been accomplished without contributions from many other people. I feel indebted and deeply grateful to them for their support.

First I would like to acknowledge and give thanks to the sources of funding which enabled this work, in particular the Brigham Young University Department of Physics and Astronomy and National Science Foundation Grant PHY-1461219I, which funded the BYU REU program I participated in during the summer of 2014.

Next, I want to express my gratitude to my research advisor, Dr. John Colton, for his continual support. While Dr. Colton was certainly ever-willing to give of his time to answer my questions and provide me needed guidance, he also was careful to allow space for me to work independently and find solutions to challenges on my own. It was clear from my first day working in his group that the well-being and success of his students is his number one priority. His influence for good will surely impact my future education and career for many years to come.

I also must thank the many others individuals with whom I have collaborated. Foremost, I need to thank Kyle Miller for his pioneering efforts with this project, undertaking much of the difficult preliminary steps to get the experiments off the ground. I am grateful for his patience and kindness while he trained me to take over for his role in the project.

I also want to thank our collaborator at the Naval Research Lab, Dr. Sam Carter, for providing samples and valuable insights into our research. I thank fellow BYU REU student researcher, Margaret Morris, for working so diligently with me over the summer of 2015 to collect the vast majority of the data presented in this thesis (it takes a patient person to be willing to spend so many hours working in the lab while be constantly bombarded by the repeating chirp of our cryostat). Lastly, I want to thank Michael Meehan for his assistance at various points along the way, including his help with the cryostat and sample preparation/placement. Most importantly though, I must thank Michael for his miraculous discovery of the journal article who's results mirror our own.

Contents

List of Figures

List of Tables

Chapter 1

Introduction

1.1 Electron Spin and Quantum Computing

Electrons have an inherent quantum mechanical property called spin. Contrary to what its name might seem to suggest, this property is not the result of electrons undergoing rotational motion. In fact, there is no direct classical analog in the macroscopic world that properly exemplifies spin. Spin can only be adequately understood through the lens of quantum mechanics. The existence of spin was determined from its two observable effects, an angular momentum and a magnetic moment. The presence of the magnetic moment in electrons results in energies levels that split in the presence of a magnetic field. This effect is commonly referred to as the Zeeman effect. Electrons, which are categorized as spin-$\frac{1}{2}$ particles, have spins that can be in either a "spin up" or a "spin down" state. An electron in the spin down state is in the higher energy state because its magnetic moment is oriented antiparallel to the field. Correspondingly, an electron with a spin magnetic moment aligned parallel to an external magnetic field is in the lower energy, or spin up, state. Because spin is a quantum mechanical property, it is potentially useful for quantum computing.

Quantum computing is the focus of much research within the scientific community today. It is a next-generational, specialized computer that would drastically reduce the time required for certain types of calculations. For example, much of modern digital encryption technology relies on the fact that traditional computers cannot compute prime factors of large integers within any reasonable amount of time. Shor's algorithm, which is only feasible on a quantum computing device, promises to drastically reduce the required computation time for such factorizations [1]. The successful implementation of such a quantum computing device would not only break current encryption methods, but it would revolutionize the world by providing means for many new computational possibilities.

1.2 Qubits

The eventual creation of a fully-functional quantum computer, while still likely many years in the future, will require the identification and implementation of qubits. A qubit is the quantum analog to the classical bit, which is currently used in traditional computing. A classical bit can represent either a 0 or a 1. The state of a classical bit is often determined physically within an electrical circuit by either a high or low voltage. A qubit is similar to a classical bit in that it requires at least a two-level system to represent 0's and 1's, but qubits are unique because they can also exploit quantum mechanical phenomena such as superposition and entanglement. Quantum superposition allows for a single quantum system to be in a combination of multiple states at the same time. For example, the spin of an electron could simultaneously be in a superposition of both the spin up and the spin down states. This unique property called superposition is perhaps the most important requirement for the implementation of the uniquely advantageous computational algorithms of a quantum computer.

There are many possible systems that could be used as qubits, such as atomic states, nuclear

spin states, or light polarizations. Electron spin states in particular have demonstrated significant potential for use as qubits. One of the major obstacles in implementing a successful spin qubit is that spin states of electrons become decoherent over time. This eventual decoherence is an inevitable result of an electron interacting with its surroundings. While such decoherence can never be entirely avoided, it is important to establish conditions for which environmental effects are limited and the coherence time will be maximized [2].

There are a few different measures of spin coherence. One of these measurements is called the T_1 time, or longitudinal relaxation time. This is a measurement of how much time is required for the spin to align itself parallel with an external magnetic field. This type of relaxation is not the kind we are most concerned with for this project. A second measurement type is called the T_2 time, or the transverse relaxation time. This is a better measure of the true coherence time for the spin states. It characterizes how quickly the spins decohere transverse to the applied magnetic field. Such transverse decoherence is the true limitation spins states in their use as a qubit. Thus there is a need to identify materials with electron spins states that have long T_2 coherence times. Silicon carbide is one such material.

1.3 Electron Spin Coherence in Silicon Carbide

Certain solid materials have shown potential for containing electron spin states with long coherence times. One such material is diamond. Diamond can contain defects called nitrogen vacancy centers, which are nitrogen atoms next to carbon vacancies. Within such defects, electrons can become localized. These localized electrons have been shown to have T_2 coherence times of up to 0.35 ms at room temperature [3]. A seperate article investigated a different diamond sample and measured coherence times at a colder temperature of 77 K, with T_2 times of 0.6 s [4]. Unfortunately diamond materials are expensive and can be difficult to manufacture. In part for such

reasons, alternative materials with similarly useful characteristics are desired. Silicon carbide (SiC) has structural similarities to diamond and has shown great potential [5].

The manufacturing methods are well developed for SiC, and it has a relatively low cost to produce. Silicon vacancy defects [6] in SiC have been shown by other researchers to have many essential characteristics needed for qubits [7]. These defects can be formed by irradiating silicon carbide with high energy particles such as electrons or protons [8]. By annealing SiC after initial defect formation, the defects can be modified to form other types of vacancies such as the silicon divacany [9]. The single silicon vacancy in SiC can be optically initiallized and read-out [10], and therefore it is particularly useful because it can be characterized by techniques such as optically detected magnetic resonance (discussed in Section 2.2).

In this thesis we investigate the silicon vacancy defect of SiC. Because the silicon vacancy in SiC appears to be a strong candidate for application as a qubit, it is necessary to understand and characterize its electron spin coherence time. We set out to measure the the T_2 times for this material and understand the key factors that limit its coherence. We measured T_2 spin coherence times across a range of temperature for two unique samples of 4H-silicon carbide that contained silicon vacancies. By making measurements over a range of temperatures and for different sample types, we can better determine how to maximize spin coherence within this material.

1.4 Previous Work Performed by Our Research Group

1.4.1 Preliminary Work and Results

This thesis is a continuation of prior work performed by our research group. Former undergraduate student Kyle Miller performed the bulk of those preliminary efforts. His work served as the foundation for this thesis and largely enabled its success. While his contributions were significant and essential to our project, most of Miller's initial results and subsequent conclusions will be shown

within this thesis to be incorrect.

Miller's work, as outlined within his senior thesis [11], involved a nearly identical investigation of electron spin coherence in SiC. He used the same spin echo technique described later in this thesis to measure spin coherence times for our precise two samples of proton-irradiated SiC. He likewise attempted to characterize the temperature dependence of the spin coherence times. Furthermore, Miller's experiments were performed with almost entirely the same laboratory equipment and data acquisition software that was used for our experiments. Miller concluded that our 10^{14} cm^{-2} proton-irradiated sample had a spin coherence time of about 20 μs and that our 10^{13} cm^{-2} proton-irradiated sample had a spin coherence time three times longer, around 65 μs (see Fig. 1.1). Kyle's results led to his conclusion that neither sample had any appreciable temperature dependence.

In one sense, Miller's findings are in agreement with our more recent results because he found that the 10^{14} cm^{-2} proton-irradiated sample had shorter coherence times than the 10^{13} cm^{-2} proton-irradiated sample. However, the similarities between the two sets of results essentially end there. The new and improved results reported in this thesis indicate much longer coherence times for both samples and a strong temperature dependence. We now attribute the inaccuracy of Miller's results to high levels of noise within his measurements. Prior to reperforming Miller's experiments, we made several improvements to the experimental set-up in order to reduce noise and increase the stability of our experimental method. These improvements are briefly described below.

1.4.2 Experimental Improvements

Magnetic Field Control

A stable magnetic field is essential for reliable measurements within this experiment. Miller employed a constant voltage power supply to power an electromagnet, which in turn created a mag-

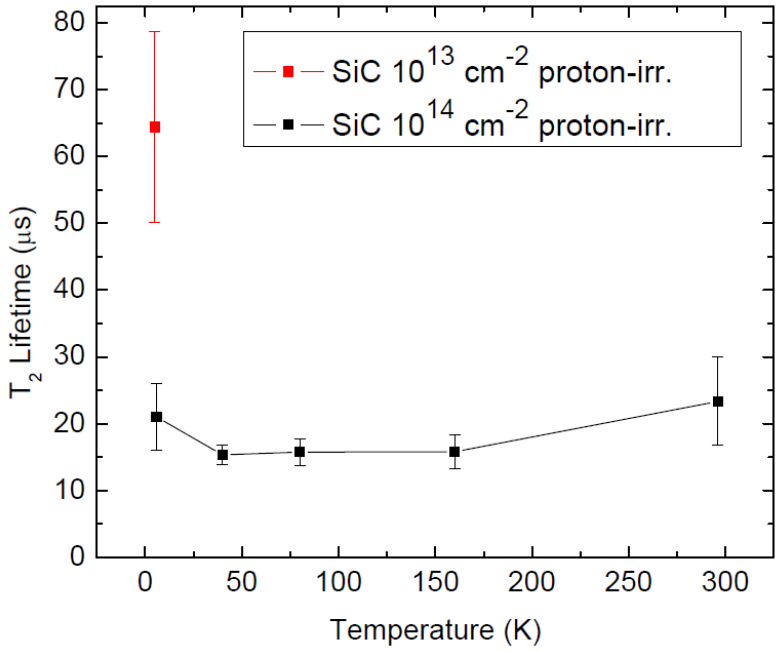

Figure 1.1 Plot indicating the preliminary measurements for spin coherence times (T_2) as measured by Kyle Miller. The black data points correspond to the coherence times of the 10^{14} cm^{-2} proton-irradiated sample, and the red data points correspond to the coherence times of the 10^{13} cm^{-2} proton-irradiated sample. While Miller only reported one value for the 10^{13} cm^{-2} sample, his published thesis indicates that other measured temperatures yielded no change in the coherence time.

netic field around the sample. The output voltage of the magnet power supply was determined by an control voltage provided from a high-precision external voltage calibrator. Unfortunately, this control scheme inevitably permitted the magnetic field strength to fluctuate and drift over time. We presume that such instabilities largely resulted from changes in temperature, and consequently internal resistance, of the magnet coils. We remedied this problem by removing the voltage calibrator from the set-up and replacing it with a gaussmeter. This gaussmeter performed two functions. First, it constantly monitored the magnetic field strength, and second, it used an internal PID controller to continually make needed adjustments to the voltage it provided to the magnet power supply. By making this change to our set-up, we observed an immense difference in magnetic field stability. Fig. 1.2 shows the stability of both magnet control methods over the course of ten minutes. Because our experiments occasionally required the collection of data over the course of 30 - 90 minutes, the improvements shown in Fig. 1.2 were essential for the success of our project. We consider this particular change to have been of greatest worth in improving the results of our data collection.

Light Filter

We used a photodiode to collect photoluminesence from our sample. When making these measurements, it is essential that no light, outside of the photoluminescence, is able to reach the photodiode. For this purpose, Miller had used two low-pass optical filters to block out any scattered laser light. We deemed it necessary to prohibit even more undesired light from hitting our detector by adding a third filter. By performing this subtle change, we increased our signal-to-noise ratio threefold, which likely contributed significantly to the successful collection of our new data set.

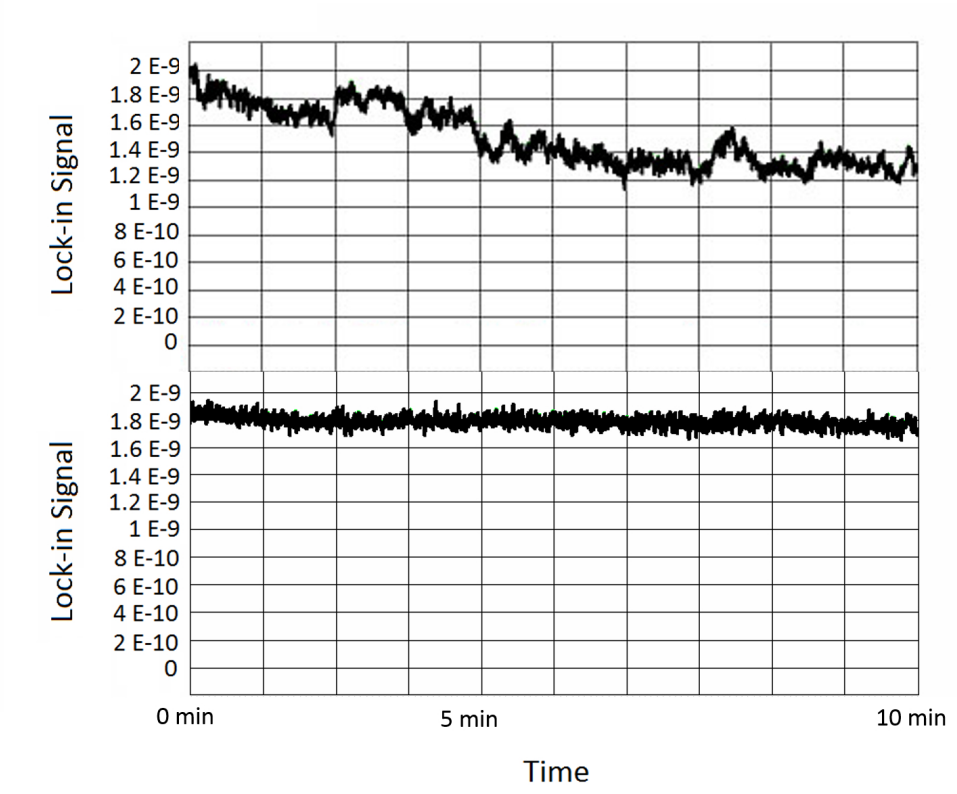

Figure 1.2 The upper graph shows the stability of the measured PL signal over the course of ten minutes when using Kyle Miller's method of controlling the magnet power supply. The lower graph shows the shows the stability when using our new method involving the gaussmeter. Note that our new method has neither strong oscillations nor an overall drift in the signal. While these plots technically show PL signal as recorded by the lock-in amplifier, they exactly mirror the changes in the magnetic field strength over the same time interval. We monitored both PL and magnetic field strength at the same time and observed perfect consistency of their fluctuations in real time, but unfortunately we did not save the magnetic field data for future display.

1.4.3 Improved Results

Having achieved a greatly improved signal-to-noise ratio, we soon discovered that we could measure much longer lifetimes than was previously possible for Miller. Our new results indicate coherence times up to three times longer than Miller's, and even more importantly, we observe a large temperature dependence. We now conclude that the high levels of noise and instability in Miller's data collection method limited the maximum coherence time that he was capable of measuring. Thus his measurements at each temperature would each reach the restrictive maximum, and he was led to falsely conclude that the spin coherence times for each sample were independent of temperature.

1.5 Overview of Thesis

The improvements that we made to our experimental set-up, as described in the previous section, allowed us to explore a few questions about electron spins in proton-irradiated 4H-silicon carbide. First, how long would the silicon vacancy electron spin states remain coherent? Second, how would temperature affect the duration of those coherence times? And third, how would the concentration of the silicon vacancies, as formed through varying amounts of proton irradiation, influence the coherence times? Each of these questions is perhaps subsidiary to the overarching question motivating our project: what are the primary factors that lead to spin decoherence in this type of material? This important question provided much of the motivation and framework for this thesis. By making spin coherence measurements under various conditions, we begin to identify the key factors which allow for maximal spin coherence.

Our experimental results for each sample indicate spin coherence times on the order of 100 μs. Each sample also has its longest coherence times at the lowest temperatures. At the temperature minimum of 8 K, one sample had a spin coherence time of nearly 300 μs. The shortest coherence

time for each sample was found at the highest temperature. Although the temperature extremes corresponded to maxima and minima in the spin coherence times, there was also a stretch of temperatures (between 60 K and 160 K) for which increased temperature led to longer spin coherence times. This unique temperature dependence defied our expectations and provides us with more questions for future research.

Chapter 2 of this thesis details the methods of our experiment. It begins with a description of the two samples of SiC which were included in the study, explaining how they were prepared, why they were useful to our project, and what distinguished each sample from the other. The two major techniques used in our experiment were optically detected magnetic resonance (ODMR) and spin echo. Chapter 2 explains each of these techniques and how they enabled us to make spin coherence time measurements. Furthermore, Chapter 2 gives an overview and schematic explanation of the instrumentation and other laboratory equipment used to perform the experiments and collect the data. Lastly, Chapter 2 includes an explanation of how the collected data was processed in order to determine spin coherence times.

Chapter 3 of this thesis gives the results obtained from the experiments. It contains figures and tables summarizing the spin coherence times for each sample across the full range of temperatures. Chapter 3 describes and discusses the observed temperature dependence of the spin coherence times that we observed. It points out consistent oscillations in the spin echo data for short spin echo scans and discusses the probable causes for which such oscillations exist. Finally, Chapter 3 puts forth the directions that this project can move towards in the future and the major questions that must now be answered as a result of our findings.

Chapter 2

Experimental Method

2.1 Silicon Carbide Samples

Two samples of high purity semi-insulating 4H-silicon carbide were provided to us by our collaborator, Dr. Sam Carter, of the U.S. Naval Research Lab. Each sample was created such that the c-axis of the crystal lattice was oriented 8° from the normal to the sample face. Both samples were irradiated with protons in order to form silicon vacancy defects in their crystal lattice structures (see Fig. 2.1). One sample was irradiated with 2 MeV protons at a fluence of 10^{13} cm^{-2} and the other with 2 MeV protons at a fluence of 10^{14} cm^{-2}. This varying degree of proton irradiation is presumed to alter the concentration of the vacancy defects that form within the sample. Thus by comparing the spin coherence times from each sample, we investigate how silicon vacancy defect concentration can contribute to the electron spin decoherence.

Carter performed Stopping and Range of Ions in Matter (SRIM) calculations to predict the stopping range for the protons inside the silicon carbide material. These calculations predicted that the stopping distance of the ions would be at about 44 μm from the sample's surface. Through empirical observations however, Carter showed that similar samples exhibit strong photolumines-

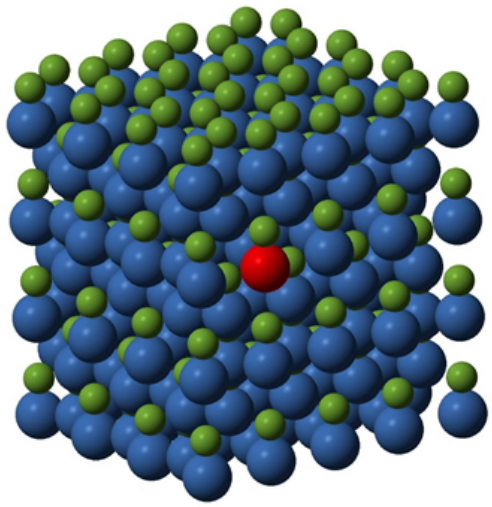

Figure 2.1 Schematic of the crystal lattice structure of 4H-SiC. Carbon atoms are represented as the smaller green spheres. Silicon atoms are represented by the larger blue spheres. The lone red sphere is representative of a missing silicon atom, or a silicon vacancy defect. The electron spin states that we investigate within this thesis are localized within these silicon vacancy defects.

cence (PL) around 915 nm, a feature indicative of the silicon vacancy of interest, near 32 μm from the surface. The amount of this PL stimulated at 32 μm was about ten times stronger than what was stimulated at other points closer to the surface. Thus the experimental results seem to show that the actual proton stopping range is most likely closer to 32 μm from the surface rather than the calculated 44 μm.

2.2 Experiment Background

2.2.1 Optically Detected Magnetic Resonance

Fig. 2.2 shows the photoluminescence (PL) response of our proton-irradiated 4H-SiC samples. Both the larger peak near 915 nm and the smaller peak near 930 nm are indicative of silicon vacancies, each corresponding to a silicon vacancy defect located at a particular location within the

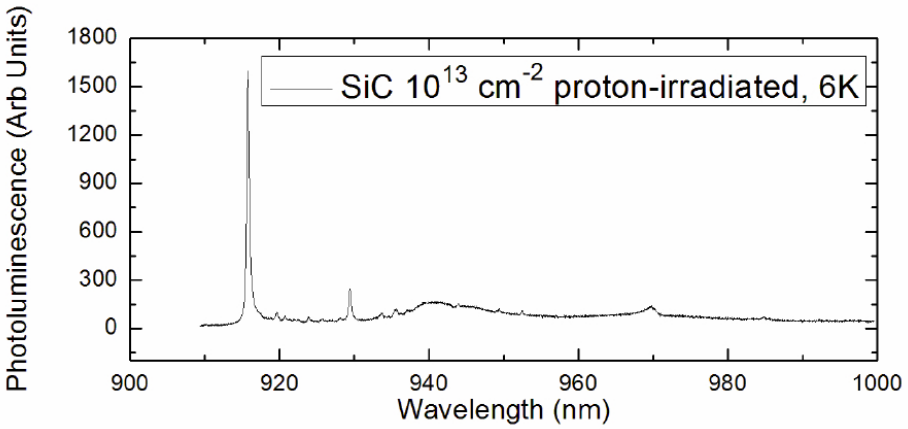

Figure 2.2 Plot showing PL vs. wavelength obtained through optically detected magnetic resonance. The peak near 915 nm is the primary peak of interest as it represents the V_2 silicon vacancy defect.

crystal lattice structure. The larger peak is accounted for by what is called the V_2 silicon vacancy defect. While two silicon vacancy sites exist, we chose to focus on the V_2 type of silicon vacancy defect for its larger PL signal. Therefore, in order to stimulate the 915 nm PL for our experiments, we tuned our pump laser to 870 nm. This value was chosen by Miller after experimenting with several possible wavelengths. He found it to be the ideal laser wavelength so as to maximize the PL response from the defects of interest and minimize the undesired PL response at different wavelengths.

When exposed to a magnetic field, the electron energy levels of different spin states are split according to the Zeeman effect. Once the energy levels are split, transitions between spin states can be induced by applying electromagnetic waves at the resonant frequency. Fig 2.3 shows two energy diagrams representative of electrons in the silicon vacancies of our samples. It is a spin-$\frac{3}{2}$ system, meaning that there are four possible spin states for the electrons and each spin state will split into a unique energy level when exposed to a magnetic field. The red lines within the left diagram in Fig 2.3 represent transitions between spins states that can be induced by resonant microwaves (which have energy equal to the separation between the two energy levels). During

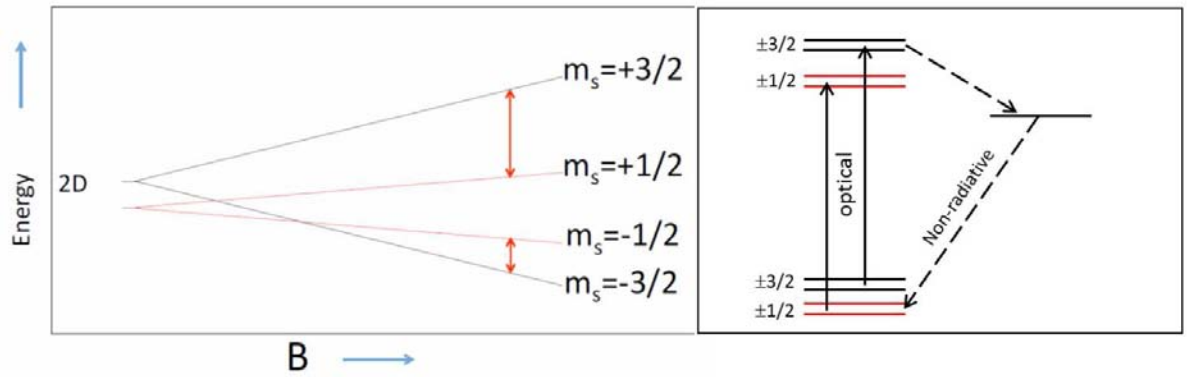

Figure 2.3 Schematic of the electron energy levels in the spin-3/2 silicon vacancies. The left-hand diagram shows how the four possible spin states split into distinct energy levels when in the presence of a magnetic field, with the red arrows indicating transitions that can be stimulated via microwaves. The right-hand diagram shows the ground and excited states for these same silicon vacancies. The electrons can be optically stimulated with a laser to move back and forth between ground and excited states, producing PL near 915 nm. Because we are pumping the electrons with linearly polarized light, these optically stimulated transitions can only occur between either the red $m_s = +1/2$ states or the black $m_s = +3/2$ states (or in other words, the electrons must maintain their same spin state when being optically stimulated between the ground and excited states). The diagram also shows a possible non-radiative transition between the excited $m_s = +3/2$ state to the ground $m_s = +1/2$ state. The existence of this non-radiative transition provides for two essential properties for our experiments: the electrons can be optically pumped, or initialized, into the $m_s = +1/2$ state and the strength of PL that we observe at any point in our experiments will vary depending on the current spin states of the electrons.

our experiments, we can apply such waves to our sample by means of a coupling loop which is formed at the end of a coaxial cable and situated directly in front of our sample.

When initially finding resonance, we pumped the sample with our laser and used a microwave generator to scan across a range of microwave frequencies until we observed a resonance peak in the PL (see Fig. 2.4). The two peaks shown in the figure for each magnetic field strength correspond to the two possible transitions between spin states identified with red arrows in Fig. 2.3. We chose to focus on the higher energy transition (between $m_s = +\frac{1}{2}$ and $m_s = +\frac{3}{2}$) for its stronger signal. Finding such resonance was accomplished by means of an Agilent Technologies E8257D microwave generator that was coupled to a Amplifier Research 20T4G18 traveling wave tube mi-

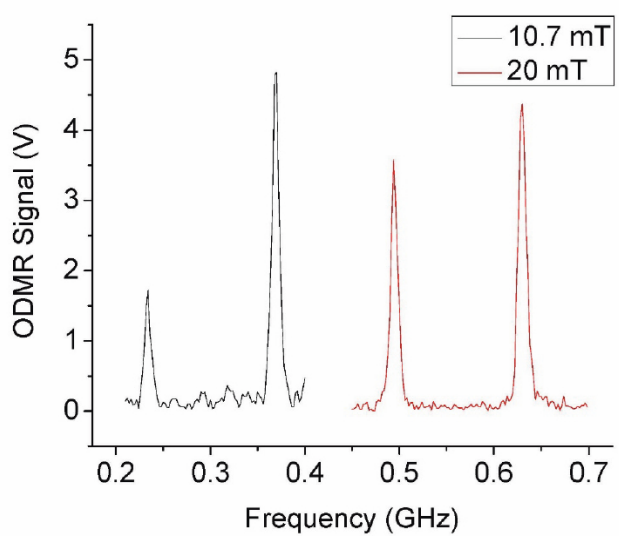

Figure 2.4 Plot showing the optically detected magnetic resonance peaks stimulated from a SiC sample. Displayed in red and black are two separate sets of resonance peaks for two different magnetic field strengths. We selected the higher of the two peaks for use within our experiment. For the field strength of 0.37 T that was eventually used in the rest of our experiments, the higher peak resonance was found at about 10.49 GHz.

crowave amplifier. The applied microwave output was chopped at a frequency of 1 kHz using a PIN diode. This on/off "gating" frequency of the chopped microwave output served as the reference frequency for the signal from our photodiode, which was received by a Stanford Instruments SR830 lock-in amplifier. We fixed the magnetic field strength (on the order of 0.37 T) and scanned across a range of microwaves (near 10.5 GHz). The resultant resonant PL is known as optically detected magnetic resonance (ODMR).

Once resonance is found, we can begin to probe the spin properties of our sample. As stated before, we chose to focus exclusively on the stimulated spin state transition between the $m_s = +\frac{1}{2}$ and the $m_s = +\frac{3}{2}$ states as represented by the upper red arrow in the left-hand diagram of Fig. 2.3. In order to simplify the following discussion, I will now begin to refer to the $m_s = +\frac{1}{2}$ spin state as the "spin up" state and the $m_s = +\frac{3}{2}$ spin state as the "spin down" state.

The right-hand diagram of Fig. 2.3 provides an illustration of how the silicon vacancy system

responds to optical excitation. We can assume that, prior to excitation with the laser light or microwaves, the ensemble of electrons begin in some random distribution of the spin up and spin down states. When we then apply an 870 nm laser pulse, transitions are stimulated between the ground and excited states. The electrons absorb incoming photons to become excited, and they emit photons (the source of our 915 nm PL) when transitioning back to down the ground state. Because of conservation of angular momentum, our linearly polarized laser light will not change the spin states of the electrons upon excitation, meaning that a spin up electron in the ground state will remain a spin up electron when optically stimulated to the exited state. There is however, a non-radiative transition that can occur from the excited spin down state to the ground spin up state. This non-radiative transition means that the optical stimulation can cause spin down electrons to become spin up electrons but not vice versa. Therefore, the initial spin state distribution will preferentially populate the spin up state upon stimulation with a laser pulse of sufficient duration. Putting this principle in practice, we used a 3 μs laser pulse in our experiments to initialize the ensemble of spins into the spin up state.

The existence of the non-radiative transition shown in Fig. 2.3 not only allows us to initialize the electrons into a known spin state, but it allows us to probe the current spin states of the electrons. If the spins are mostly aligned in the spin up state, we will observe a large amount of PL because mostly radiative transitions will occur. If the spins are mostly aligned in the spin down state, a smaller amount of PL will result because some of the electrons will undergo the non-radiative transition.

2.2.2 Rabi Oscillations

Fig. 2.5 shows how the measured PL from optical stimulation varies depending on the spin state of the electrons. Seen in this figure are Rabi oscillations, or the cycling back and forth between two possible spin states. As shown in the pulse diagram inset in the same figure, we first pulse

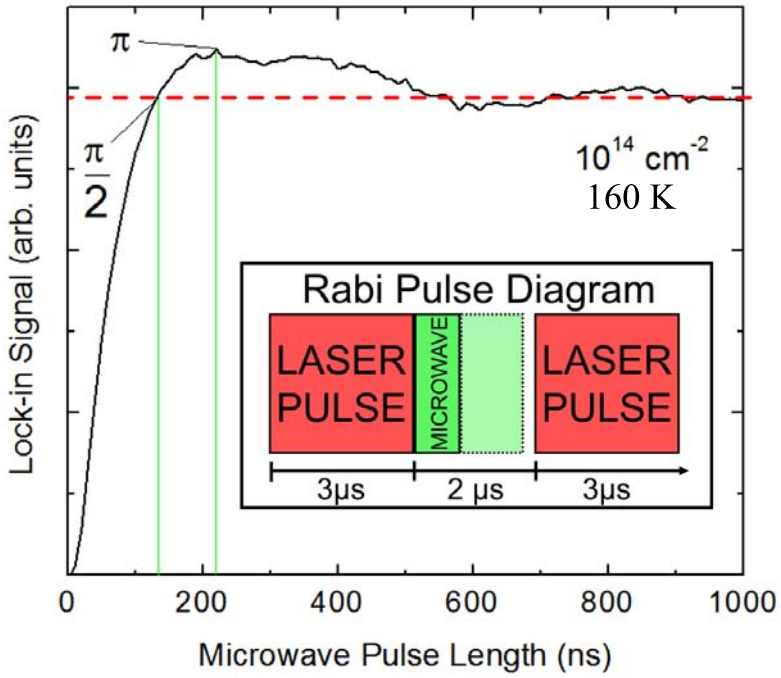

Figure 2.5 Plot of the Rabi oscillations induced by varied microwave pulse durations. This scan was performed on the 10^{14} cm^{-2} proton-irradiated sample at 160 K. The $\pi/2$ and π pulse lengths are identified with vertical green lines. The dashed red line is the asymptotic value that is approached for long microwave pulses. Inset: Rabi pulse diagram showing the order and relative lengths of the laser and microwave pulses.

the sample for 3 μs to initialize the electrons into the spin up state. Then we begin to apply microwave pulses of varying lengths, from 0 ns to around 2000 ns. These microwave pulses cause the spin states to gradually transition, from the spin up state, into a superposition of both states, to the spin down state, back into a superposition, and eventually back to original spin up state. Fig. 2.5 shows how the photoluminescence oscillates up and down throughout this process. Again, such oscillations results from the non-radiative transition possible from the excited spin down state (shown in Fig. 2.3).

It is apparent in Fig. 2.5 that the oscillations begin to die out for longer microwave pulse lengths. This dampening is mostly caused by dephasing that occurs among the ensemble of electrons in the direction perpendicular to the static magnetic field. Much like tiny bar magnets exposed to a

magnetic field perpendicular to their orientation, the complex phase of electron spins will precess in a magnetic field. The rate of this precession can vary for each electron in the probed ensemble. The time required for this dephasing is called the T_2^* time. The T_2^* time does not represent the true limit of coherence because the dephasing effects can be accounted for with methods such as spin echo (described in the next section). The more meaningful T_2 time will always be longer than the T_2^* time.

By observing the microwave pulse length necessary for the PL signal to reach its first maximum, we can deduce the π-pulse length, or the microwave pulse length needed to rotate the electron spins from one state to another (a 180° rotation). In a similar way, we can look for the microwave pulse length for which the PL first reaches its asymptotic value in order to deduce the pulse length required to rotate the spins 90° into an equal superposition of the spin up and spin down states. This second pulse duration is called the $\frac{\pi}{2}$-pulse length. Observing the Rabi oscillations and determining the durations of these two pulse types is essential in order to perform our spin echo experiment.

2.2.3 Spin Echo

The primary technique we used to determine the spin coherence times is called spin echo. In this technique we exploit the fact that the amount of stimulated photoluminescence varies according to the spin state of the electrons. Spin echo is performed by means of a sequence of laser and microwave pulses. First, we again align the spins into the spin up state by applying a 3 μs laser pulse. We then apply a $\frac{\pi}{2}$ microwave pulse, which causes the spins to rotate 90° into an equal superposition of the two possible states. Next, we wait for a time delay (t_{fixed}) and allow for the spins to precess in the x-y plane of the Bloch sphere. Because we are probing an ensemble of spins, each will precess at a different rate. To overcome the effects of this dephasing, we apply a second microwave pulse, this time a π-pulse. This second microwave pulse rotates the spins

another 180° into second equal superposition of the spin states, but now it's a superposition with opposite orientation in the complex planex-y plane of the Bloch sphere. After waiting a second time delay (t_{varied}), the ensemble of spins will precess back together. We then apply a second $\frac{\pi}{2}$-pulse to rotate the spins another 90° back into their original spin up state. The degree to which the spins remain coherent throughout this microwave pulse sequence determines how well they will be aligned back into their initial state in the end. If they are well aligned back into the spin up state, it will result in a smaller amount of photoluminescence. This dip in photoluminescence that occurs when the spins are well aligned is called the "echo". By performing these spin echo scans for longer and longer time delays, we inevitably observe the coherence of the spin states decay. Fitting the spin echo coherence data to an exponential decay curve, we can determine the exponential decay constant, which represents the spin coherence time at each temperature. Fig. 2.6 shows a spin echo pulse diagram, some example spin echo data, and the sloped Gaussian fit.

2.3 Experiment Set-Up

2.3.1 Cryostat and Temperature Control

In order to probe the temperature dependence of the spin coherence times, we placed the sample inside a nonmagnetic CryoIndustries cryostat. This cryostat is capable of adjusting the temperature of the sample from room temperature down to around 8 K. In order for the cryostat to successfully reach such a low temperature, we used a turbopump vacuum system to pump down the cryostat chamber to around 10^{-4} mbar. To achieve intermediate temperatures (anywhere between room temperature and 8 K), we heated the system with an integrated heater coil powered by a temperature controller with PID functionality. By varying the amount of current applied through this heater and simultaneously cooling the system with the cryostat pump, we could reach and maintain any desired intermediate temperature.

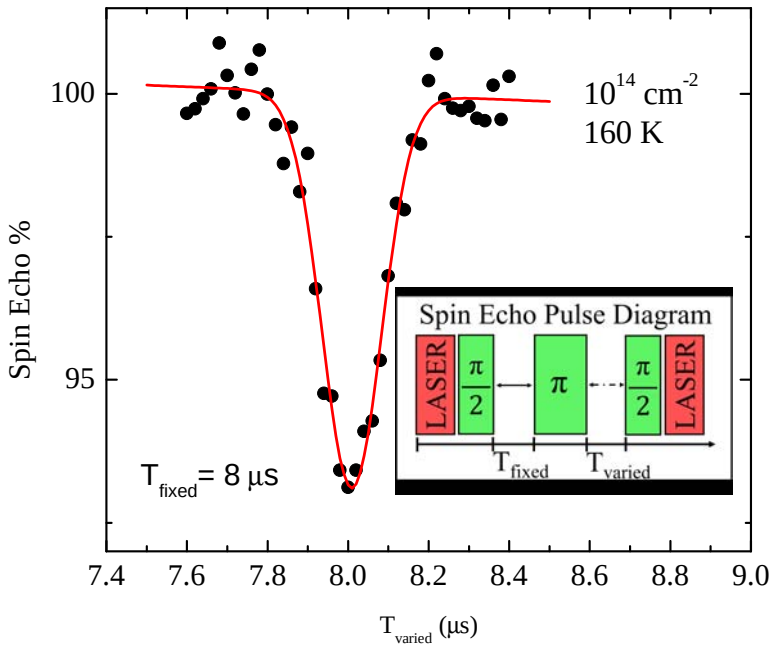

Figure 2.6 Spin echo data for a scan with a T_{fixed} value of 8 μs. This scan was performed on the 10^{14} cm^{-2} proton-irradiated sample at 160 K. The black circles represent the collected data points. The red line is a sloped Gaussian function that is fitted to the experimental data. Inset: Spin echo pulse diagram. This schematic shows the order of laser pulses, microwave pulses, and time delays used in the spin echo technique.

2.3.2 External Static Magnetic Field

Our external magnetic field was provided by means of a large conventional iron-core electromagnet situated around the cryostat. This electromagnet produced a static magnetic field at about 0.37 T. The electromagnet itself was powered by a Magna-Power Electronics TS Series IV power supply in constant voltage mode, and it was cooled by flowing water lines. In order to ensure that the magnetic field remained stable over the course of our long spin echo scans, it was necessary to monitor the field strength using a gaussmeter. We placed a Lakeshore DSP 750 gaussmeter probe near the sample and constantly measured the magnetic field strength over time. The gaussmeter has a variable voltage output which is set by an internal PID controller and can be used to supply a control voltage to a power supply. Thus, we connected the voltage output of the gaussmeter to the control voltage input of our magnet power supply. Using its own built-in PID controller functionality, the gaussmeter constantly monitored the magnetic field strength and made fine adjustments to the power supply control voltage in order to ensure that the magnetic field strength remained steady over the course of time.

2.3.3 Microwave generation and amplification

The microwaves necessary for our experiments were generated by an Agilent Technologies E8257D microwave generator set to 10.4855 GHz at 0 dBm. This generator was coupled to a Amplifier Research 20T4G18 traveling wave tube microwave amplifier which amplified the microwaves about 40 dBm. The microwave frequency near 10.49 GHz was selected in order to maximize the output power of the microwaves. The majority of the work in establishing ideal microwave power was performed by Kyle Miller [11], so one can look to his published thesis for more detailed information. In brief, Kyle used a stub tuner prior to the microwave coupling loop in order to ensure maximum microwave transmission from the amplifier.

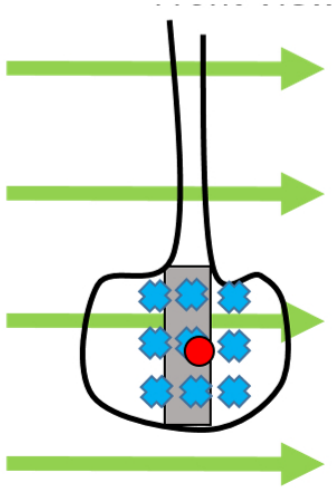

Figure 2.7 Diagram of the coupling loop and magnetic fields at the sample. The sample itself is represented by the grey rectangle. The coupling loop is represented by the black loop. The laser hitting the sample is represented by the red circle. The green horizontal arrows indicate the direction of the external static magnetic field provided by the electromagnet. The blue crosses represent the magnetic field due to the microwaves emitted by the coupling loop. These blue magnetic field lines point into the page, perpendicular to the external magnetic field.

2.3.4 Microwave Coupling Loop

A coupling loop, used to transmit microwaves from the microwave amplifier/generator, was placed directly in front of the sample in order to manipulate the spin states in the sample. The orientation of this coupling loop was such that the emitted microwaves would apply a magnetic field perpendicular to that of the static magnetic field (shown in Fig 2.7). Thus the application of microwaves from the coupling loop could alter the spin orientation by causing electron spin states to transition back and forth. For example, applying microwaves to spins aligned in the spin up state would cause the spins to transition into a superposition of the spin up and spin down states. Once the spin orientation was misaligned with the static magnetic field, the complex phase of the new spin alignment would precess.

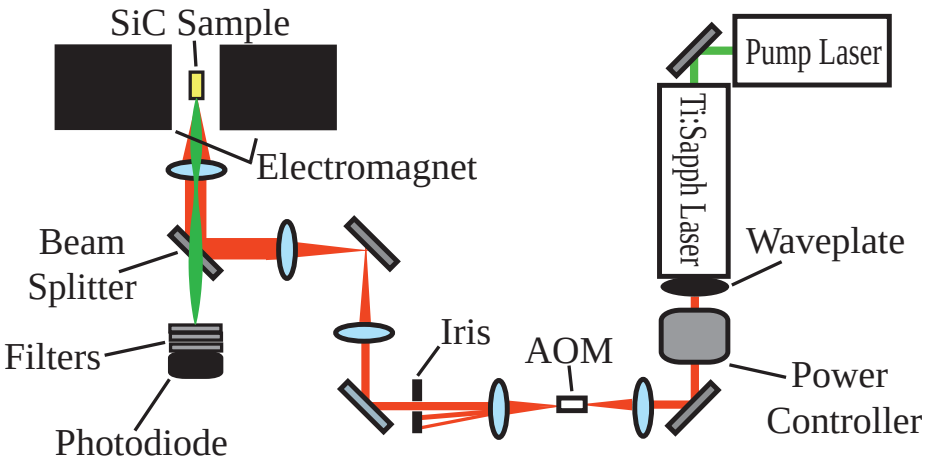

Figure 2.8 Optical set-up. A diode laser (532 nm) powers a Ti:Sapph laser, which is tuned to 870 nm and stabilized by a laser power controller. An acousto-optic modulator (AOM) modulates the laser light. After passing through the iris, the light goes through a series of telescoping lenses to expand the beam, eventually allowing for a smaller beam waist when focused by the lens situated directly in front of the sample. The beam splitter initially reflects the incoming laser light towards the sample, and upon return, it only allows for the longer-wavelength photoluminescence from the sample to pass through. Three filters block out even more of the remaining laser light from reaching the photodiode.

2.3.5 Ti:Sapph Laser and Optics

In order to perform spin echo, the electron spins must first be placed into a known initialization state (in this case the $m_s = +\frac{1}{2}$, or spin up state). This initialization was accomplished by means of optical pumping with a laser and a series of optics. Fig. 2.8 shows this optical set-up, including the PL collection optics and equipment. The laser was a cw Spectra-Physics 3900 S Ti:Sapph laser that was powered by a 532 nm diode pumped solid state laser, tuned to a 870 nm wavelength, and directed into a small point on the sample (about 50 μm in diameter).

In order to maintain a consistent laser intensity at the sample, the laser first passed through a Brockton Electro-Optics Corp BEOC laser power controller. This device receives input laser light and continuously adjusts the amount of laser light it outputs in order to maintain a constant power. Prior to entering the device, the light must be vertically polarized. We therefore placed a half-wave plate along the optical path prior to the power controller in order to rotate the horizontally-polarized

laser light into a vertical orientation.

As explained in the previous section, our experiments require a laser that can be pulsed for short periods at precise points in time. While the desired patterns can easily be created with a digital pulse generator, we needed a mechanism that could quickly modulate the laser on and off according to that generated sequence. For such purposes, we used a NEOS Technologies 15210 acousto-optic modulator (AOM). This device contains a piezoelectric crystal. The crystal can be vibrated at a particular frequency, which causes the index of refraction within the crystal to be altered in a precise manner. This alteration makes it such that when the laser passes through the crystal it forms a diffraction pattern. Using an iris, we selected the first-order beam from this diffraction pattern and blocked out the rest of the unwanted light. Thus, when the AOM was on, a diffraction pattern was created and most of the beam continued onward toward our sample, but when the AOM was off, the beam was entirely blocked by the iris. We used this method to apply 3 μs laser pulses at frequencies from around 10 kHz to 200 kHz.

After passing through the iris, the light goes through a series of telescoping lenses to expand the beam, eventually allowing for a smaller beam waist after being focused by the lens situated directly in front of the sample. The beam splitter (Thor Labs Dichroic Mirror, Long Pass 900 nm, DMLP900R) initially reflects around 90% of the incoming laser light towards the sample, and upon return, it only allows about 90% for the longer-wavelength photoluminescence from the sample to pass through. Three long pass filters (2 of which are Edmund Optics 900 nm long pass filters, Stock No. #66-237) each block out around 99.9% of the remaining laser light from reaching the photodiode, while allowing the desired PL to transmit with about 90% efficiency. The photodiode receives the PL and provides a signal to the lock-in amplifier.

Stimulated PL from the sample was focused through a lens and directed through three low-pass optical filters, each filter designed to remove extraneous laser light by attenuating all light of wavelengths longer than 900 nm. This filtered PL was then collected by a photodiode connected

to a lock-in amplifier. The reference frequency for the lock-in amplifier was determined by the frequency of the gated microwave pulse sequences. Thus we could observe the amount of PL that was emitted during the pulse sequences.

2.4 Data Processing

After obtaining the experimental data from the spin echo experiments, several more steps were required in order to arrive eventually at the spin coherence times (T_2). We fit a Gaussian peak with a linear baseline to each collection of spin echo data and determined the percent change in the signal from an extrapolated baseline to the point of maximum spin echo response. This sloped Gaussian curve fit was performed on normalized data as shown in Fig. 2.6. We use this same fit for each spin echo scan (each scan representing a unique T_{fixed} value) and determine the percent change from the fit.

Plotting the spin echo data for a variety of spin echo sequence lengths, we observed the gradual decoherence and determined the exponential decay constant of the data. When we plot the spin echo percent vs. T_{fixed}, the T_2 spin coherence time is twice of the exponential decay constant that we would determine from an exponential decay fit because the T_{fixed} time represents only half of the full microwave pulse sequence (in the equations that follow below I have taken the liberty of adding this factor of two into the decay function). We initially attempted to fit all of the decay data to a single exponential decay function, but it became apparent that such a fit did not always appropriately characterize the data. It was therefore necessary to find the next simplest fitting function to characterize the data in such cases. We found that the data for the 10^{14} cm^{-2} proton-irradiated sample fit well to a stretched exponential decay function, $y = A\ exp[-(\frac{2T_{fixed}}{T_2})^n]$. This type of exponential decay function represents a continuous distribution of decay times where n is a parameter that characterizes the distribution of the decay times. While such a function did

appear to fit well to most of this sample's data, a biexponential function fit equally as well. The biexponential was of the form $y = A_1 e^{-2\mathrm{T}_{fixed}/\mathrm{T}_{2short}} + A_2 e^{-2\mathrm{T}_{fixed}/\mathrm{T}_{2long}}$, where T_{2short} and T_{2long} represent two different decay times within the spin population. Because both fits worked well, we could not distinguish which one was better, and so we report the values found from both methods.

Unfortunately, these two types of fits were only possible for one of our samples, the 10^{14} cm^{-2} proton-irradiated sample. The data for the other sample had too much noisy inconsistency to be reliably fit with those functions. We could not definiteivly say that this data could fit best to anything other than a more simple single exponential decay function, $y = Ae^{-2\mathrm{T}_{fixed}/\mathrm{T}_2}$. The single and stretched exponential fit types can be seen in Fig. 2.9. From the parameters determined by these fits, we determine the coherence times reported in Chapter 3.

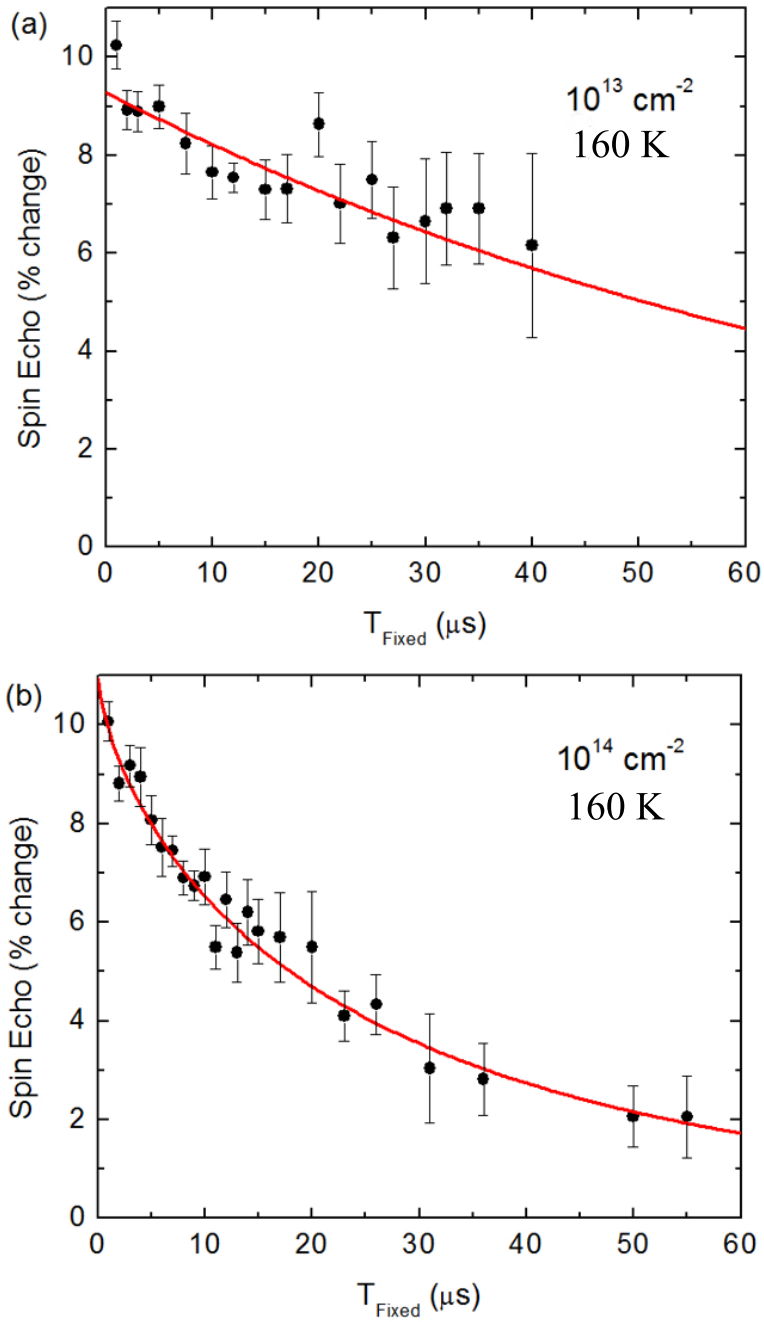

Figure 2.9 Examples of the exponential decay seen in the spin echo for both samples types. Part (a) is for the 10^{13} cm^{-2} proton-irradiated sample and is fitted to a single exponential function (shown in red). This decay fit yielded a T_2 time of about 164 μs. Part (b) is for the 10^{14} cm^{-2} proton-irradiated sample and is fitted to a stretched exponential function (shown in red). This decay fit yielded a T_2 time of about 51 μs. All data shown was collected at 160 K.

Chapter 3

Results

3.1 Electron Spin Coherence Times Summary

We successfully collected data for both SiC samples across a wide range of temperatures. The intent was to make measurements for each sample from 8 K to room temperature, but high levels of noise in the 10^{13} cm^{-2} proton-irradiated sample prohibited us from reliable data collection above 190 K. While the data set is unaviodably smaller for the 10^{13} cm^{-2} proton-irradiated sample, we still have sufficient data to observe trends and make comparisons between the two samples.

Table 3.1 and Table 3.2 give the T_2 coherence times for both the 10^{13} cm^{-2} and the 10^{14} cm^{-2} proton-irradiated SiC samples. The coherence times for the 10^{14} cm^{-2} sample were determined by a stretched exponential curve fit and a biexponential fit as described in the previous chapter. Due to higher levels of noise in the 10^{13} cm^{-2} sample, we could not definitively make the claim that the exponential decay was best represented by anything other than a single exponential decay function.

Fig. 3.1 is a graphical representation of the data presented in Table 3.1 and Table 3.2.

Table 3.1 Electron spin coherence times (T_2) and corresponding uncertainties at various temperatures for the 10^{13} cm^{-2} proton-irradiated SiC sample.

Temperature (K)	T_2 (μs)
8	270 ± 61
20	110 ± 55
30	105 ± 28
40	45 ± 10
60	69 ± 14
90	41 ± 8
120	55 ± 11
160	164 ± 30
190	32 ± 9

Table 3.2 Electron spin coherence times (T_2) and corresponding uncertainties at various temperatures for the 10^{14} cm^{-2} proton-irradiated SiC sample.

Temperature	Stretched Exponential Fit		Biexponential Fit	
(K)	T_2 (µs)	n	T_{2short} (µs)	T_{2long} (µs)
8	79 ± 6	0.6 ± 0.1	8 ± 5	104 ± 17
12	70 ± 3	0.7 ± 0.1	9 ± 5	90 ± 8
20	34 ± 11	0.4 ± 0.1	1.1 ± 0.4	62 ± 5
30	28 ± 3	0.7 ± 0.1	6 ± 4	43 ± 7
40	21 ± 3	0.6 ± 0.1	1 ± 1	32 ± 2
60	8 ± 3	0.4 ± 0.1	2 ± 1	28 ± 3
80	9 ± 5	0.4 ± 0.1	3 ± 1	30 ± 6
120	34 ± 3	0.6 ± 0.1	7 ± 3	62 ± 12
160	51 ± 4	0.7 ± 0.1	12 ± 9	77 ± 21
190	32 ± 6	0.5 ± 0.1	2 ± 1	63 ± 5
220	30 ± 3	0.7 ± 0.1	2 ± 1	40 ± 4
295	22 ± 5	0.5 ± 0.1	5 ± 3	47 ± 14

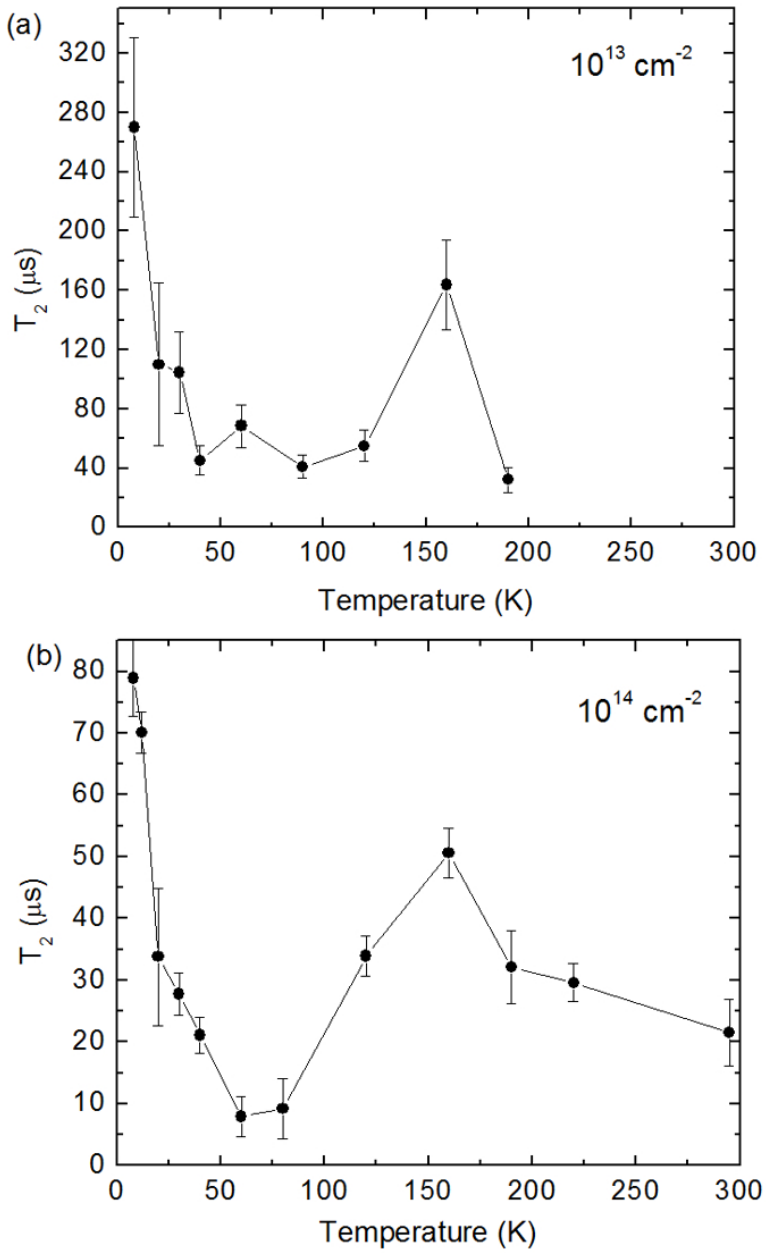

Figure 3.1 Spin coherence times vs. temperature for each sample of SiC. The 10^{13} cm^{-2} proton-irradiated sample has no data points higher than 190 K because the signal became too noisy at that point. The black connecting lines serve only as guides to the eye between the data points.

3.2 Temperature Dependence of the Coherence Times

Our primary motivation for making measurements across a range of temperatures was to understand how changes in temperature would influence the spin coherence times. Such an understanding can give insight into the main sources of the gradual spin decoherence, allowing for better design and fabrication of future materials. Prior to making measurements on our samples, we expected one of two possibilities: (1) coherence times would decrease with temperature, or (2) coherence times would be independent of temperature. The observed results defied our expectations.

It is easily observed that the coherence times are indeed dependent upon temperature. In an overall sense, we observe the expected decline in coherence time with temperature, however, that trend is not observed throughout the entirety of the temperature range. There exists a range of temperatures from about 60 K to 160 K for which the measured coherence times increase with increased temperature.

3.3 Short Pulse Sequence Oscillations

Another interesting, albeit somewhat unrelated, feature of the spin echo results is oscillations in the spin echo scans for short pulse sequences (t_{fixed} values less than about 5000 ns). These oscillations are shown in Fig. 3.2. One can distinctly observe the spin echo signal oscillate up and down. These oscillations occur simultaneously with the overall exponential decay that occurs for longer pulse sequences. The observed oscillations are consistent and reproducible even at different temperatures. These oscillations are likely a result of interactions between the electron spins and the nuclear spins. There is a naturally present, yet small, percentage of ^{29}Si and the ^{13}C isotopes that can give rise to such effects.

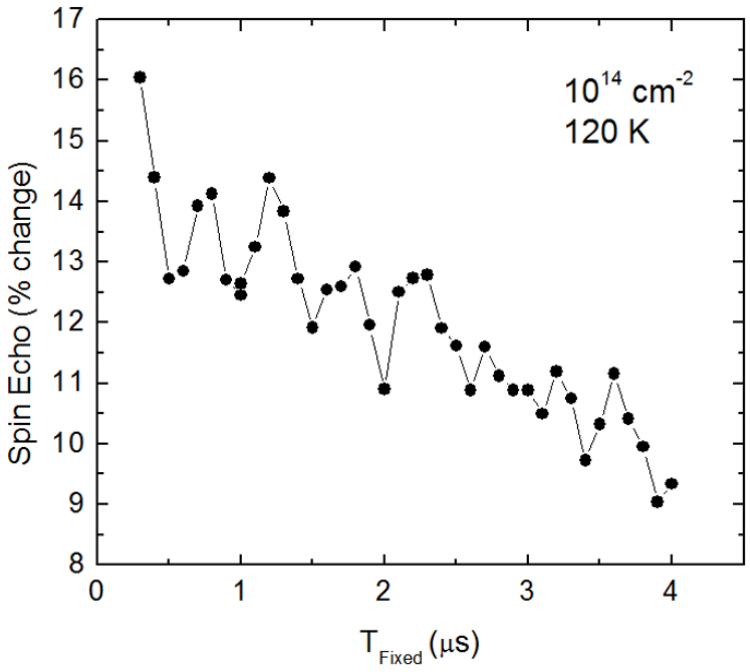

Figure 3.2 Plot of the spin echo for short microwave pulse sequences. The observed oscillations were consistent across different temperatures.

3.4 Conclusions and Future Work

The primary conclusion of our project is that the electron spin coherence times for our samples are highly dependent upon temperature. There exists a range of temperatures for which the lifetimes increase with temperature. This result, although unanticipated, is not without precedent. Falk et al. [12] observed a strikingly similar trend while measuring T_2^* electron spin times in silicon divacancies of 6H-SiC. While their results were not taken for an identical sample or defect type, the similarity of their results reaffirms the validity of our findings and suggests that there is a common underlying cause. Unfortunately Falk et al. was unable to offer much of an explanation for the interesting trend. We at this point are unable to explain it either. Our unexpected results now give us an important question to answer moving forward.

Future work in extension of this project should include further work with similar materials. For

example, our collaborator Sam Carter has provided us with another 4H-SiC sample, but this new sample has been irradiated with electrons rather than protons. By making similar measurements for a variety of samples, we can compare results and make more definitive conclusions about the strongest sources of decoherence and the impact of changes in temperature.

Whatever direction the future may take, the work presented in this thesis leaves us with one particularly important question that must be answered: why is there an increase in spin coherence times across a portion of the temperature range? The unexplained results (shown in Fig. 3.1) were consistent for two unique samples and were very similar to a result found by others [12] for a different sample and defect type, thus we are confident that the unique trends are not merely coincidence. It is exciting to have identified an unexplained physical result, and we are anxious to further investigate its cause.

Bibliography

[1] P. W. Shor, "Polynomial-Time Algorithms for Prime Factorization and Discrete Logarithms on a Quantum Computer," SIAM J. Comput. **26,** 1484–1509 (1997).

[2] C. H. . D. D. Bennett, "Quantum information and computation," Nature pp. 247–255 (2000).

[3] S. Prawer and A. D. Greentree, "Diamond for Quantum Computing," Science **320,** 1601–1602 (2008).

[4] N. Bar-Gill, L. M. Pham, A. Jarmola, D. Budker, and R. L. Walsworth, "Solid-state electronic spin coherence time approaching one second," Nature Communications **4,** 1743 (2013), diamond.

[5] P. G. Baranov, A. P. Bundakova, A. A. Soltamova, S. B. Orlinskii, I. V. Borovykh, R. Zondervan, R. Verberk, and J. Schmidt, "Silicon vacancy in SiC as a promising quantum system for single-defect and single-photon spectroscopy," Physical Review B **83,** 125203 (2011), diamond.

[6] E. Sörman, N. T. Son, W. M. Chen, O. Kordina, C. Hallin, and E. Janzén, "Silicon vacancy related defect in 4H and 6H SiC," Phys. Rev. B **61,** 2613–2620 (2000).

[7] V. A. Soltamov, A. A. Soltamova, P. G. Baranov, and I. I. Proskuryakov, "Room Temperature Coherent Spin Alignment of Silicon Vacancies in 4*H*- and 6*H*-SiC," Phys. Rev. Lett. **108,** 226402 (2012).

[8] H. Itoh, N. Hayakawa, I. Nashiyama, and E. Sakuma, "Electron spin resonance in electron-irradiated 3C-SiC," Journal of Applied Physics **66,** 4529–4531 (1989).

[9] W. E. Carlos, N. Y. Garces, E. R. Glaser, and M. A. Fanton, "Annealing of multivacancy defects in 4*H*-SiC," Phys. Rev. B **74,** 235201 (2006).

[10] P. G. Baranov, A. P. Bundakova, A. A. Soltamova, S. B. Orlinskii, I. V. Borovykh, R. Zondervan, R. Verberk, and J. Schmidt, "Silicon vacancy in SiC as a promising quantum system for single-defect and single-photon spectroscopy," Phys. Rev. B **83,** 125203 (2011).

[11] K. G. Miller, "Electron Spin Echo and Coherence Times in Silicon Carbide Defects," Brigham Young University Department of Physics and Astronomy (2015).

[12] A. L. Falk, P. V. Klimov, V. Ivády, K. Szász, D. J. Christle, W. F. Koehl, A. Gali, and D. D. Awschalom, "Optical Polarization of Nuclear Spins in Silicon Carbide," Phys. Rev. Lett. **114,** 247603 (2015).

Index